Applied Physics A (2022) 128:284
https://doi.org/10.1007/s00339-022-05450-y

Applied Physics A
Materials Science & Processing

RAPID COMMUNICATIONS

Shallow trap mediated charge transport in polymer dielectrics for HVDC by incorporating 2D nanoclay

Mohamadreza Arab Baferani[1,2] · Chuanyang Li[1,2] · Yang Cao[1,2]

Received: 29 January 2022 / Accepted: 28 February 2022

Abstract

In this letter, we report a new space charge suppression solution for polymer dielectrics by a manner of incorporating 2D Talc nanoclay particles to enhance shallow trap mediated charge transport. This approach was verified in both semi-crystalline cross-liked polyethylene (XLPE) and amorphous cross-linked ethylene propylene rubber (EPR), with large performance improvement independent of the crystalline morphology of polymers. The introduction of 2D Talc nanoclay modifies the distribution of the traps in polymer with enlarged number of shallow states, effectively increasing the charge carrier mobility while significantly reducing the macroscopic activation energies for XLPE from 0.88 to 0.66 eV and for EPR from 0.97 to 0.54 eV, as indicated by the quasi steady-state conduction measurement. The shallow trap mediated charge transport was further investigated by the Thermally Stimulated Depolarization Current (TSDC) measurement, confirming the decrease in the activation energy from 0.99 to 0.54 eV for XLPE and from 1.02 to 0.52 eV for EPR. The resulting higher mobility of charge carriers in the nanocomposite samples with 2D Talc nanoclay contributes to a notable suppression of the heteropolar space charge, and consequently, a huge reduction of the local electric field enhancement, from 60 to 15% for XLPE and 31.5–11% for EPR, when tested at 50 °C with the presence of a thermal gradient. This trap-mediated charge transport study unveils a new approach for HVDC cabling with high scalability for future renewable energies.

Keywords Charge transport · HVDC insulators · Polymer dielectric · Shallow traps · Space charge · 2D nanoclay

1 Introduction

Polymer dielectrics, such as cross-linked polyethylene (XLPE) and ethylene propylene rubber (EPR), have been widely used as the insulators for high voltage equipment [1–3]. However, the development of the polymer dielectrics for high voltage direct current (HVDC) cable insulation remains a challenging task for both scientific researchers and engineers due to the complexity and interplays of strongly temperature dependent electrical conductivity and accumulation of trapped space charges in polymers [4, 5]. Suppressing space charge has been regarded as the most critical issue of HVDC insulation [6–8], and many material modification solutions have been proposed. Tailoring the bulk properties of polymer matrix by introducing inorganic nanoparticles has been reported with performance enhancement via space charge suppression. For instance, the introduction of surface-treated silica nanoparticles in LLDPE [6], ZnO nanoparticles in PE [9], NaY zeolite in PE [10], poly (stearyl methacrylate)-grafted SiO_2 nanoparticles in XLPE [11], and MgO nanoparticles in PVDF [12] have already been studied. However, these studies are based on the suppression effect of the introduced deep traps for efficient charge capturing near the electrode-dielectric interface so as to reduce the electric field next to the electrode to block the charge injection. These approaches are inherently prone to voltage polarity reversal and may lead to insulation failure in emerging Smart-Grids with topologies like multi-terminal DC designed for distributed, clean, and renewable energies integration. In this work, we report a trap modulation approach based on the shallow traps introduced by incorporating large interface 2D nanoclay in polymer dielectrics for superior DC characteristics. Representative polymer dielectrics of XLPE and EPR, with one being semi-crystalline and the other amorphous, are employed as the base materials to

✉ Yang Cao
yang.cao@uconn.edu

[1] Electrical and Computer Engineering Department, University of Connecticut, Storrs, CT 06269, USA

[2] Electrical Insulation Research Center, Institute of Materials Science, University of Connecticut, Storrs, CT 06269, USA

Published online: 12 March 2022

showcase the effectiveness of this novel shallow-trap modulation approach in the suppression of space charge accumulation as well as the tuning of temperature coefficient of electrical conductivity, two most critical characteristics for HVDC insulations.

2 Experimental details

PE and EPR with peroxide cross-linkers were prepared and incorporated with a 40% weight ratio of 2D Talc nanoclay. Samples denoted by XLPE-P, XLPE-C, EPR-P, and EPR-C stand for the pure XLPE, the Talc-filled XLPE, the pure EPR, and the Talc-filled EPR, respectively. The samples were hot-pressed at 120 °C and 9 tons pressures for 10 min to prepare plaques with desired thickness. After that, the samples were cross-linked at 165 °C and 5 tons pressures for 15 min to complete the cross-linking process. A Thermo Fisher Verios scanning electron microscopy (SEM) was utilized to investigate the morphology of the samples. X-ray diffraction (XRD) spectroscopy was applied to study the crystalline morphology of the samples qualitatively. To characterize the thermal behavior of the samples and compare the level of crystallinities, differential scanning calorimetry (DSC) scans from −80 to 220 °C with 10 °C/min rate of heat flow were used.

The dielectric spectroscopy was measured using an IMASS time-domain dielectric spectrometer (TDDS). A Laplace transformation was applied to the results to convert the data in the time domain to frequency response. The TDDS measurements were performed utilizing a stainless-steel guarded electrode configuration with an electrode diameter of 2.54 mm and the thickness of samples is ~1 mm [13]. The pulse electroacoustic (PEA) was utilized to characterize the charge density distribution of the samples under DC electric field. For PEA measurement, the samples with a thickness of ~ 250 µm were prepared and coated with 60/40 weigh% Au/Pd sputter coatings on both sides [13]. The space charge was measured under 20 kV/mm at 25 °C and at 50 °C with 1 °C/mm thermal gradient (TG) across the samples in parallel with the direction of applied electric field to simulate the load condition in actual cable. The electric field distribution across the samples because of space charge accumulation was calculated using the Gauss's law as presented by $E(x) = \frac{1}{\varepsilon_0 \varepsilon_r} \int_0^x \rho(x) dx$, where $\rho(x)$ is the charge density, $E(x)$ is the electric field, ε_0 is the vacuum permittivity, and ε_r is the relative permittivity of the material. The electrical conductivity was measured by employing a three-terminal sample holder built in accordance with the ASTM 257 Standard inside of an oven to control the ambient temperature. The polarization current data were recorded via a Keithley 6514 electrometer for 2000 s and the average of current density at 1900–2000 s was used to calculate the conductivity. Thermally stimulated depolarization current (TSDC) was measured to evaluate the trapping characteristics of the samples. For TSDC, the sample was heated to 80 °C and poled at 20 kV/mm for 120 min. Then, with the electric field still applied, the sample was cooled to − 80 °C. Finally, the electrodes were short-circuited and the current in the circuit was measured during the reheating of the sample with a rate of 3 °C/min up to 130 °C.

3 Results and discussion

Figure 1a–d shows the cross section of the samples. It can be found from Fig. 1a and b that the pure samples appear uniform with compact texture without defects. Figure 1c and d verified that 2D Talc nanoclay were distributed uniformly across the polymer matrix of XLPE and EPR in parallel with the surface of the samples. In Fig. 1e, the diffraction peaks of XLPE-P and EPR-P at 2θ~21° and the major peaks of the 2D Talc nanoclay at 2θ ~9.8°, 18.9°, 28.5°, 48.8°, and 59.3° have been verified favorable to the incorporated 2D Talc nanoclay. It should be noted that XLPE-P has a sharper peak compared with the wide peak of EPR-P, which is due to the semi-crystalline morphology of XLPE in comparison with the amorphous structure of EPR. In Fig. 1f, the DSC spectra for the heating curves, the XLPE-based samples have a peak at 100 °C, which is attributed to the change of crystallinity from crystalline to amorphous structure in the semi-crystalline XLPE. The glass transition of the EPR-based samples was observed around − 50 °C. In addition, the peak at 50 °C in the EPR-based samples is related to the small crystallinity of the EPR polymer as related to the ratio of ethylene to propylene in the EPR structure. The pure samples have crystallinity peak with higher amplitude compared with the filled nanocomposites of the same polymer due to the higher amount of crystalline polymer chains in a same weight.

Considering the first peak of 2D Talc nanoclays at 2θ ~9.8° and using Bragg's law, $d = \frac{n\lambda}{2sin\theta}$, where n is the diffraction order (1, 2, 3, 4, …), θ is the x-ray incident angle, and λ is the wavelength of x-ray for Cu anode,1.54 nm, [14] the inter-planar spacing or d is 9.01 Å. Therefore, each elementary sheet of Talc layer which is composed of a layer of magnesium-oxygen/hydroxyl octahedra, sandwiched between two layers of siliconoxygen tetrahedral has a thickness of ~2.7 nm. Using SEM, the average thickness of stacks of 2D Talc nanoparticles are ~200–300 nm. This means each stack includes on average ~70–110 Talc sheets. The 2D nanoclay particles incorporated into polymer matrix are oriented parallel with the surface of the plaque. Considering a uniform and oriented distribution of 2D nanoclay particles inside of the polymer matrix, in a micro-scale volume of the composite as presented in

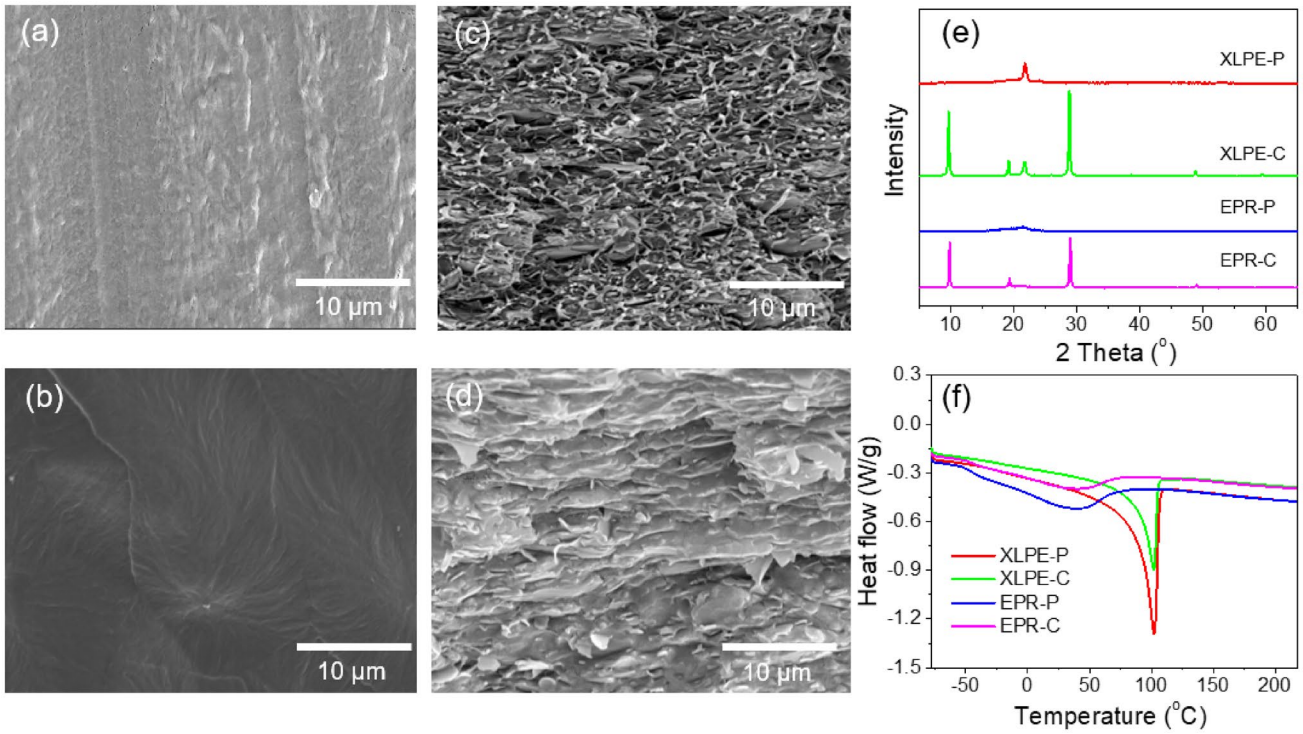

Fig. 1 (**a**) cross section of XLPE-P, (**b**) cross section of EPR-P, (**c**) cross section of XLPE-C, (**d**) cross section of EPR-C, (**e**) XRD spectra, and (**f**) DSC spectra

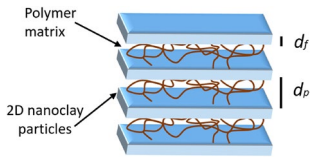

Fig. 2 Schematic presentation of 2D nanoclay particles in polymer matrix

Fig. 2, the surface area is similar between the 2D nanoclay and polymer matrix. Therefore, the distance between the particles is in direct relation with the volume of polymer matrix as presented by Eq. (1),

$$\frac{d_f}{d_p} = \frac{V_f}{V_p} = \frac{(w_f/\rho_f)}{(w_p/\rho_p)} \tag{1}$$

where d_f is the average thickness of particles, d_p is the average space between particles, V_f is the filler volume, V_p is the polymer volume, w_f is the weight ratio of filler, w_p is the weight ratio of polymer, ρ_f is the density of filler, and ρ_p is the density of polymer. Considering 40%, 60%, 2.7 (g/cm^3), and 1.2 (g/cm^3) as the weight ratio of filler, the weight ratio of polymer, the density of filler, and the density of polymer, respectively, the ratio of particles' thickness to the distance between particles is ~0.3. Therefore, the average distance between particles is ~666–1000 nm.

Dielectric constant and dissipation factor of the pure and the nanocomposite samples in the frequency range of 0.01–10,000 Hz at room temperature are presented in Fig. 3. The dielectric constant and dissipation factor of the samples increase with incorporation of 2D nanoclay particles into the polymer matrix as shown in Fig. 3a and b, respectively. The reason is the presence of interfacial polarization or Maxwell–Wagner polarization in the nanocomposite samples. Difference in electrical characteristics of polymer and 2D nanoclay particles in the nanocomposite samples leads to a buildup of charge at the interface between the particles and polymer under applied electric field, and the loss peaks at lower frequencies present this type of polarization [15, 16].

The charge distribution across the XLPE-based samples is depicted in Fig. 4. Figure 4a presents the charge distribution of XLPE-P at 25 °C. A hetero-polar charge cluster with the amplitude of ~ 7.5 C/m^3 was accumulated adjacent to the cathode. The electric field distribution of XLPE-P is shown in Fig. 4b where the hetero-polar charge results in a local electric field enhancement (EFE) up to 28 kV/mm, a 40% enhancement of the nominal field, next to the cathode. The charge accumulation became worse at 50 °C with TG, as shown in Fig. 4c, and the extension of positive charge

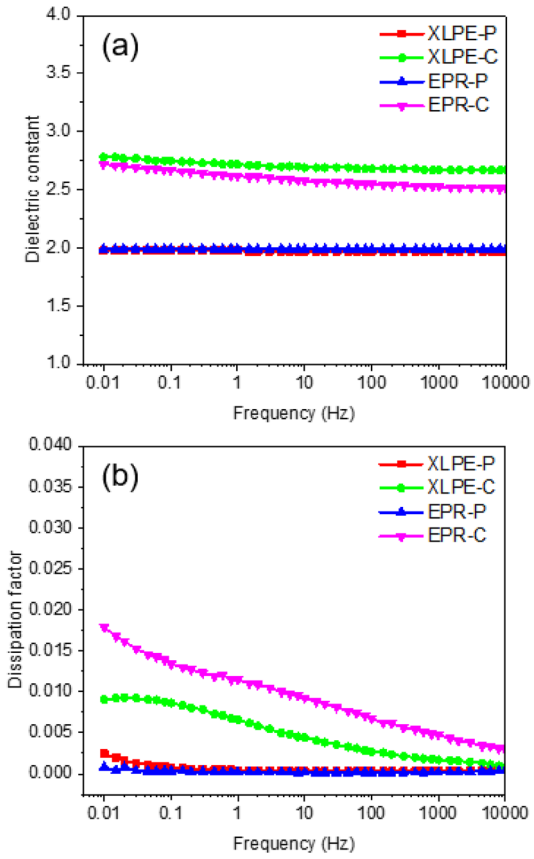

Fig. 3 (**a**) Dielectric constant, and (**b**) dissipation factor of the studied samples in the frequency range of 0.01–10,000 Hz at room temperature

clusters can be observed from the middle of sample (0.5 P.U.) to near the cathode (0.1 P.U.) with a maximum density of 7.7 C/m^3. Therefore, this exacerbates the electric field distortion next to the cathode up to 32 kV/mm, 60% higher than the nominal field, as presented in Fig. 4d. The charge accumulation at 25 °C was suppressed in XLPE-C as shown in Fig. 4e and it makes the electric field significantly uniform with the maximum amount of 21.4 kV/mm, an EFE of only 7% (Fig. 4f). With temperature rise and TG, a tiny amount of injected negative charge close to the cathode as homo-polar charge can be observed in Fig. 4g. Due to the suppression of hetero-polar charge across the bulk, the electric field distribution of XLPE-C is uniform and without any notable electric field enhancement with the maximum electric field of 23 kV/mm, an EFE of only 15% (Fig. 4h).

Measured at a similar condition to XLPE-P, EPR-P shows significant amount of accumulated charge across the sample, spreading from the middle to close to the cathode with the maximum density of 4.4 C/m^3 next to the cathode (Fig. 5a). This charge accumulation especially the hetero-polar charge adjacent to the dielectric-electrode interfaces accounts for the local EFE of 28.8 kV/mm, 44%, as depicted in Fig. 5b. At 50 °C with TG, the accumulated positive charge extended across the sample with the maximum density of 6.7 C/m^3 at the position of 0.6 P.U., as shown in Fig. 5c. This charge accumulation augments the electric field locally next to the cathode, with a maximum electric field of 26.3 kV/mm, an EFE of 31.5% (Fig. 5d). Compared with EPR-P, EPR-C exhibits outstandingly suppressed hetero-polar charge accumulation at both temperatures, as shown in Fig. 5e and g. The maximum density of the accumulated charge is less than 2 C/m^3 at 25 °C, and 2.2 C/m^3 at 50 °C with TG, respectively. The resulting uniform electric field distribution in EPR-C with a maximum electric field of 21.8 kV/mm or an EFE of only 9% at 25 °C, and 22.2 kV/mm or an EFE of only 11% at 50 °C with TG, as shown respectively in Fig. 5f and h, clearly indicates the suppression of space charge under not only low (current) load condition, but more importantly, the emulated high load condition with a temperature gradient across the polymer dielectric that often induces hetero-polar charge. Such huge improvement is attributed to this unique shallow-trap modulation approach with the incorporation of 2D platelet Talc nanoclay, as will be further revealed in the underlying mechanism studies of temperature dependent electrical conductivity and TSDC characterizations.

The conductivity of the samples can be found in Fig. 6a and b. The presented results have been measured for three different fresh samples and the error bar shows the standard deviation from the average. The conductivity values increased with electric field and temperature. The conductivity of the EPR-based samples appears to be higher than the XLPE-based samples under the measured conditions. For example, the conductivity of the samples with XLPE as the polymer changes in the range of 1.28×10^{-16}–5.43×10^{-15} S/m at 25 °C; however, for the EPR-based samples it alters from 3.33×10^{-16} S/m to 1.24×10^{-14} S/m. This could be due to the lower bandgap of EPR, i.e., ~ 6–7 eV [17], compared with that of XLPE polymer which is about 8.5 eV [18]. In addition, EPR has a more amorphous structure with inherently more disordered structures than the semi-crystalline XLPE [19]. This causes the larger amount of localized states or Anderson states and accordingly higher conductivity of the EPR-based samples than XLPE-based ones.

The other salient observation from conductivity results is the lower dependency of conductivity to electric field in the nanocomposite samples compared with the pure ones at both temperatures. The conductivity of XLPE-P varies from 1.62×10^{-16} under 10 kV/mm to 4.62×10^{-15} S/m under 40 kV/mm at 25 °C; however, it is in the range of 3.28×10^{-16}–1.55×10^{-15} S/m for XLPE-C. Also, EPR-P has a remarkable variation of conductivity (about two orders) with increasing electric field from 3.89×10^{-16} to 1.23×10^{-14} S/m at 25 °C. On the other hand, EPR-C has only a moderate conductivity rise from 3.64×10^{-15} to 4.67×10^{-15} S/m with the electric field rise. The same

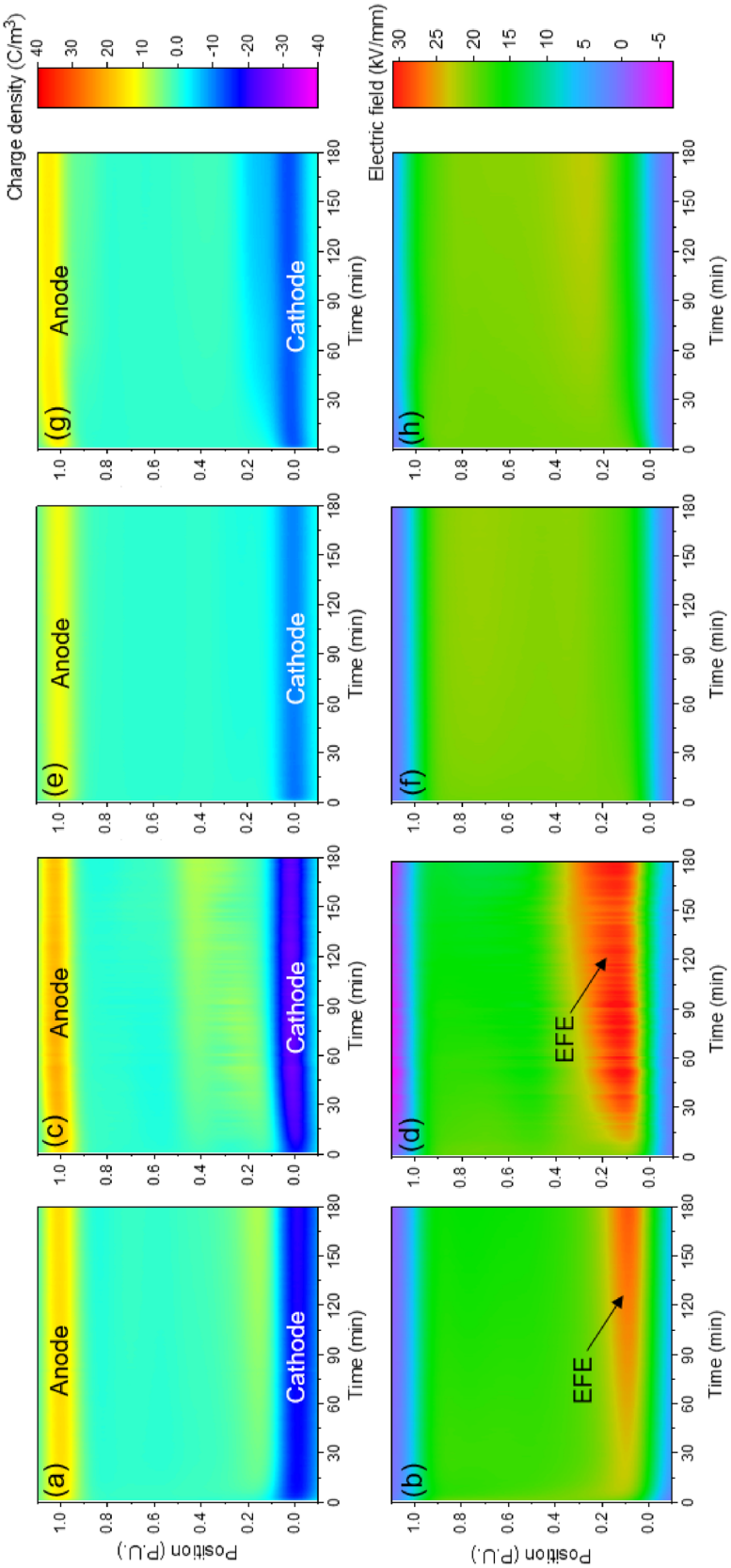

Fig. 4 Top: charge density profile and bottom: electric field distribution of (**a**)-(**b**) XLPE-P at 25 °C, (**c**)-(**d**) XLPE-P at 50 °C with TG, (**e**)-(**f**) XLPE-C at 25 °C, and (**g**)-(**h**) XLPE-C at 50 °C with TG. The vertical axis shows the position across the sample in per unit (P.U.), and the horizontal axis presents the time of measurement in minutes

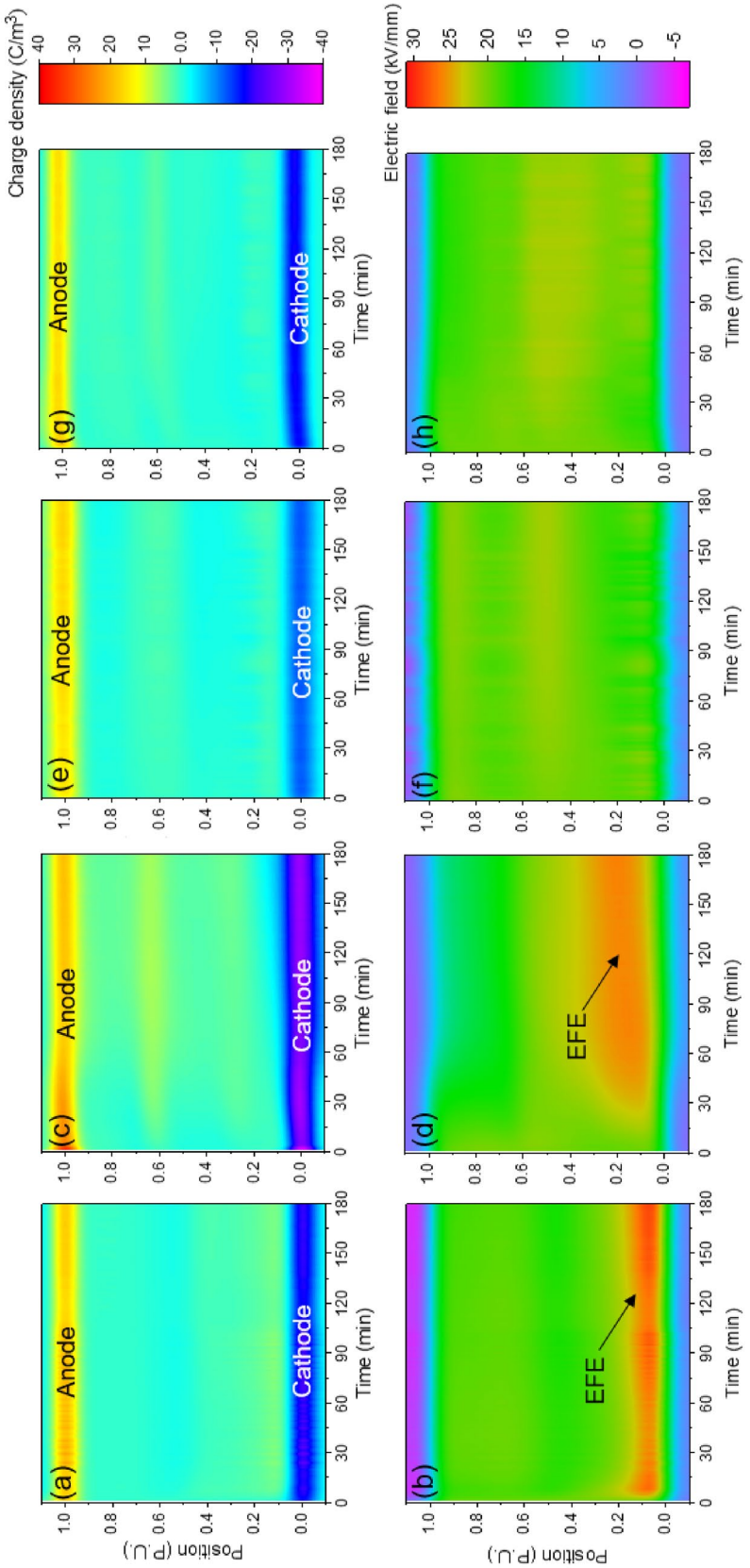

Fig. 5 Top: charge density profile and bottom: electric field distribution of, (**a**)-(**b**) EPR-P at 25 °C, (**c**)-(**d**) EPR-P at 50 °C with TG, (**e**)-(**f**) EPR-C at 25 °C, and (**g**)-(**h**) EPR-C at 50 °C with TG. The vertical axis shows the position across the sample in per unit (P.U.), the horizontal axis presents the time of measurement in minutes

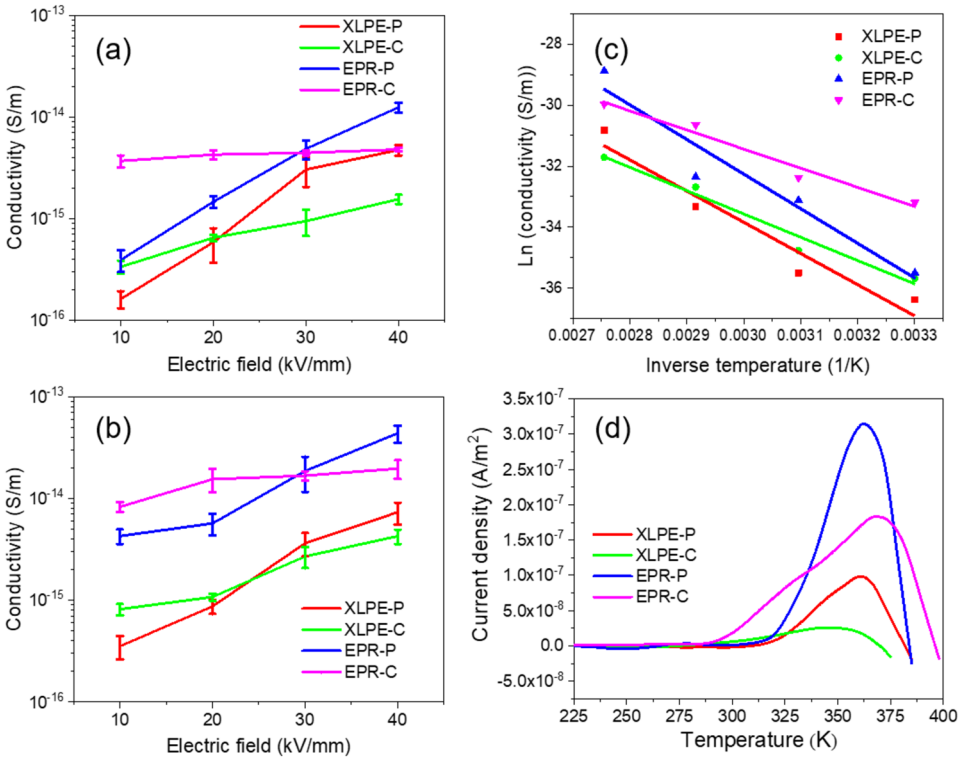

Fig. 6 (**a**) Electrical conductivity at 25 °C, (**b**) electrical conductivity at 50 °C, (**c**) Arrhenius plots for the conductivities at 10 kV/mm on temperature range of 30–90 °C, and (**d**) TSDC spectra

condition is relevant at higher temperature where the conductivity of the XLPE-P and EPR-P modify notably (more than one order) in the range of 3.57×10^{-16}–7.35×10^{-15} S/m and 4.19×10^{-15}–4.27×10^{-14} S/m, respectively. Nevertheless, the conductivity rise is still smooth for the nanocomposite samples. The conductivity of XLPE-C changes between 8.12×10^{-16} and 4.14×10^{-15} S/m and EPR-C alters between 8.37×10^{-16} and 1.98×10^{-15} S/m. The electric field dependency of conductivity in dielectrics is related to the mean distance between the traps [2, 20]. This suggests that, when the density of the shallow traps involved in charge transport increases and consequently the average distance between the traps decreases, the dependency of conductivity to electric field reduces. Therefore, the density of the shallow traps should be higher in the nanocomposite samples compared with the pure ones.

The dependency of conductivity to temperature is characterized by evaluating the activation energy of conductivity and follows the Arrhenius equation as presented in Eq. (2),

$$\sigma(T) = \sigma_0 exp\left(\frac{-\varphi}{kT}\right) \tag{2}$$

where σ_0 is the conductivity at infinite temperature (S/m), φ is the activation energy (eV), k is the Boltzmann's constant (eV/K), and T is the absolute temperature (K). The logarithmic version of Arrhenius equation is a straight line often used to fit the experimental results and reach activation energy. Figure 6c presents the Arrhenius plots of the conductivities at different temperatures from 30 to 90 °C at 10 kV/mm. The slope of the fitted plots, the solid lines, represents the activation energy, which is considered as the hindrance against charge carriers' mobility and could allude the average effective depth of the traps in bulk of dielectric. Thus, the higher dependency of conductivity to temperature and hence higher activation energy of conductivity indicates the higher average depth of the traps. The measured activation energies for XLPE-P, XLPE-C, EPR-P, and EPR-C are 0.88, 0.66, 0.97, and 0.54 eV, respectively. With respect of activation energy, it is suggested that the average depths of the traps in XLPE-C and EPR-C are correspondingly lower in comparison with XLPE-P and EPR-P. Moreover, the profound reduction in the activation energy results in in the nanocomposite samples not only higher charge carrier mobility and lower dielectric time constant ($\tau=\varepsilon/\sigma$), but also highly suppressed space charge and modulated conductivity with lower temperature dependence.

The TSDCs as a function of temperature have been measured and presented in Fig. 6d. To study the TSDC results and calculate the activation energy, a curve fitting method [21] was used. The measured depolarization current density $J(T)$ is related to activation energy w as described in Eq. (3),

$$J(T) = A\exp\{-\frac{w}{kT} - \frac{B}{b}\int_{T_0}^{T}\exp\left(-\frac{w}{kT'}\right)dT'\} \tag{3}$$

where T *and* $T^{'}$ are temperatures [K], T_0 is the initial temperature [K], b is the heating rate [K/s], and A [A/m^2] and B [1/s] are adjustable parameters [21, 22]. In the fitting process, the nonlinear Levenberg–Marquardt algorithm was used and the reduced chi-square and adjusted r-square values were controlled to obtain the optimal parameters. The fitted curve of the peak for the studied samples have been presented in Fig. S1-S4 in the supplementary file. The resulted activation energy is 0.99 eV for XLPE-P and 0.54 eV for XLPE-C. The significant decrease in the activation energy shows the decrease in the average trap depth and the effective energy barrier against de-trapping process for XLPE-C compared with XLPE-P. The higher amplitude of depolarization current at higher temperatures is attributed to the higher density of the deeper traps and the higher amount of trapped charges in the bulk of XLPE-P compared with XLPE-C. EPR polymer shows a similar behavior with the activation energy of 1.02 eV for EPR-P and 0.52 eV for EPR-C. Therefore, the nanocomposite samples have a shallower average trap depth in comparison with the pure samples. The large interface of 2D Talc nanoclay particles with the polymer matrix and its interfacial characteristics modified the distribution of the traps by introducing shallow traps, a tuning of the trap modulated charge transport. This effect was also explained and verified by the dependency of conductivity to electric field and temperature.

4 Conclusion

In summary, we demonstrated that the incorporations of 2D Talc nanoclay into the semi-crystalline XLPE and amorphous cross-linked EPR both leads to the space charge suppression especially the hetero-polar charge accumulation under DC electric field. The lower amount of accumulated charge contributes to the more uniform electric field distribution and a significant reduction in maximum local EFE for the nanocomposite samples under not only low (power) load but also high load condition that imposes a thermal gradient across the cable insulation. The uniformly distributed 2D Talc nanoclay with large interface with polymer matrix altered the distribution of the traps to introduce a larger amount of shallow states. The growth of the shallower traps density causes higher charge carrier mobility which alters the electrical conduction characteristics. In addition, the activation energies measured by both quasi steady-state electrical conduction and TSDC are lower for the samples with 2D Talc nanoclay which confirms the lower average trap depth and lower energy barrier against charge carrier transport in these nanocomposite samples and thus elucidates the mechanism of space charge suppression. The results of this study unveil a new pathway for the design of novel polymer-based nanocomposites for the HVDC insulators.

Supplementary Information The online version contains supplementary material available at https://doi.org/10.1007/s00339-022-05450-y.

Acknowledgements This work was supported by Kerite, Okonite, Electrical Cable Compounds, Lion Elastomers and ExxonMobil and partially by NSF under the grant 1650544. The authors also thank JoAnne Ronzello for help with the experimental setting-up.

References

1. X. Qi, S. Boggs, IEEE Electr. Insul. Mag. **22**(3), 19–24 (2006)
2. M.A. Baferani, C. Li, M. Tefferi, N. Wang, Y. Cao, J. Phys. D: Appl. Phys. **54**(47), 475304 (2021)
3. G.C. Montanari, M. Xu, D. Fabiani, L.A. Dissado, Appl. Phys. A **107**(3), 539–551 (2012)
4. M. Tefferi, M.A. Baferani, H. Uehara, Y. Cao, IEEE Access **8**, 187840–187847 (2020)
5. L.S. Cardoso, G.E. Gonçalves, D.H.F. Kanda, R.F. Bianchi, H.N. Nagashima, Appl. Phys. A **123**(12), 1–9 (2017)
6. X. Huang, P. Jiang, Y. Yin, Appl. Phys. Lett. **95**(24), 242905 (2009)
7. Q. Cheng, J.W. Zha, J.T. Zhai, D.L. Zhang, X. Bian, G. Chen, Z.M. Dang, Appl. Phys. Lett. **115**(10), 102904 (2019)
8. Y. Liu, L. Li, X. Du, Appl. Phys. A **8**(2), 757–762 (2015)
9. F. Tian, Q. Lei, X. Wang, Y. Wang, Appl. Phys. Lett. **99**(14), 142903 (2011)
10. B. Han, X. Wang, Z. Sun, J. Yang, Q. Lei, Appl. Phys. Lett. **102**(1), 012902 (2013)
11. L. Zhang, M.M. Khani, T.M. Krentz, Y. Huang, Y. Zhou, B.C. Benicewicz, L.S. Schadler, Appl. Phys. Lett. **110**(13), 132903 (2020)
12. Y. Shi, L. Zhang, J. Zhang, H. Zhang, Z. Yue, Appl. Phys. Lett. **116**(17), 172902 (2020)
13. M.A. Baferani, C. Li, T. Shahsavarian, J. Ronzello, Y. Cao, IEEE Trans. Dielectr. Electr. Insul. **28**(1), 223–230 (2021)
14. H. Khan, A.S. Yerramilli, A. D'Oliveira, T.L. Alford, D.C. Boffito, G.S. Patience, Can. J. Chem. Eng. **98**(6), 1255–1266 (2020)
15. S. Paul, T.K. Sindhu, IEEE Trans. Dielectr. Electr. Insul. **21**(2), 460–466 (2014)
16. M.A. Baferani, C. Wu, Y. Cao, Compos. Sci. Technol. **219**, 109241 (2022)
17. J. Li, B. Du, J. Su, H. Liang, Y. Liu, Polymers **10**(5), 500 (2018)
18. P. Geng, J. Song, M. Tian, Z. Lei, Y. Du, AIP Adv. **8**(2), 025115 (2018)
19. G. Blaise, J. Electrostat. **50**(2), 69–89 (2001)
20. M.J.P. Jeroense, F.H. Kreuger, IEEE Trans. Dielectr. Electr. Insul. **2**(5), 718–723 (1995)
21. R.M. Neagu, E.R. Neagu, I.M. Kalogeras, A. Vassilikou-Dova, Mater. Res. Innov. **4**(2–3), 115–125 (2001)
22. J. Van Turnhout, Electrets, in *Topics in Applied Physics*, vol. 33, ed. by G.M. Sessler (Springer, Berlin, 1980)